Exsolution Synthesis of Nanocomposite Perovskites with Tunable Electrical and Magnetic Properties

BNL-222714-2022-JAAM

Exsolution Synthesis of Nanocomposite Perovskites with Tunable Electrical and Magnetic Properties

J. Wang, I. Waluyo

To be published in "Advanced Functional Materials"

November 2021

Photon Sciences

Brookhaven National Laboratory

U.S. Department of Energy

USDOE Office of Science (SC), Basic Energy Sciences (BES) (SC-22)

DISCLAIMER

Exsolution synthesis of nanocomposite perovskites with tunable electrical and magnetic properties

Jiayue Wang[1], Komal Syed[2], Shuai Ning[3], Iradwikanari Waluyo[4], Adrian Hunt[4], Ethan J. Crumlin[5], Alexander K. Opitz[6], Caroline A. Ross[3], William Bowman[2], Bilge Yildiz[1,3]*

[1]Department of Nuclear Science and Engineering, Massachusetts Institute of Technology, Cambridge, MA, USA

[2]Department of Materials Science and Engineering, University of California, Irvine, CA USA

[3]Department of Materials Science and Engineering, Massachusetts Institute of Technology, Cambridge, MA, USA

[4]National Synchrotron Light Source II, Brookhaven National Laboratory, Upton, NY, USA

[5]Advanced Light Source, Lawrence Berkeley National Laboratory, Berkeley, CA, USA

[6]Institute of Chemical Technologies and Analytics, TU Wien, Vienna, Austria

* e-mail: byildiz@mit.edu

ABSTRACT

Nanostructured functional oxides play an important role in enabling clean energy technologies and novel memory and processor devices. Using thin-film $La_{0.6}Sr_{0.4}FeO_3$ (LSF) as a model system of technological importance, we show the novel utility of exsolution in fabricating self-assembled metal oxide nanocomposites with tunable functionalities. Exsolution triggers the formation of metallic iron (Fe^0) nanoparticles, Ruddlesden-Popper domains, and nm-scale percolated Fe-deficient channels in LSF. Combining multimodal characterization with numerical modeling, we assessed the chemical, magnetic, and electrical properties of the exsolution-synthesized nanocomposite at different stages of Fe^0 exsolution as well as during redox cycling. After exsolution, the electronic conductivity of the nanocomposite LSF increased by more than two orders of magnitude. Based on numerical analysis representing all the constituents, we expect this increase in conductivity to originate mainly from the Fe-deficient percolating channels formed during exsolution. Moreover, the exsolved nanocomposite is redox-active even at moderate temperatures. Such redox capabilities can enable dynamic control of the nanocomposite functionality by tailoring the oxygen non-stoichiometry. We demonstrate this concept with a continuous modulation of magnetization between 0 and 110 emu/cm^3. These findings point out that exsolution may serve as a platform for scalable fabrication of complex metal oxide nanocomposites for electrochemical and electronic applications.

Introduction

Nanocomposite oxides[1-4] have been considered as a promising platform to optimize the electronic[5], mass/ion transport[6-9], magnetic[10], and catalytic[11] properties of the materials. For example, integration of metallic phases into the oxide matrix has been used to increase the electronic conductivity in solid oxide cells (SOCs)[12], as well as to improve the uniformity in resistive switching[13-15]. It is desirable to develop scalable synthesis methods that can precisely control the chemical and structural features, and thereby the functional properties of the nanocomposites.[3,16]

Exsolution is a partial decomposition process where metallic nanoparticles are precipitated out of the host metal-oxide matrix upon thermal or electrochemical reduction[17-20]. Compared to nanoparticles prepared by deposition or impregnation[21], the exsolved nanoparticles have three unique advantages: First, exsolution can generate nanoparticles both on the surface[17-20,22] and in the interior[15,22-25] of host oxides. Such flexibility makes exsolution a powerful method to fabricate nanostructures at specific, otherwise inaccessible locations in the devices. Second, the exsolved nanoparticles can either reintegrate into the host oxide[19,26-28], or reversibly oxidize at their initially exsolved locations[24,29,30]. This reversible red-ox ability opens up the possibility to switch functional properties of the materials during operation[19,30,31]. Finally, for catalytic applications, the anchored sturcture[18] of the exsolved nanoparticles on the surface makes them highly stable against particle coarsening and aging[29].

While exsolution has been extensively employed to enhance surface catalytic properties[19,23,30,32,33], its potential to modulate bulk properties remains open. In fact, given that the original application has been in catalysis, bulk exsolution has been considered as an undesirable process[27,28]. Herein, we propose that exsolution can provide new opportunities in synthesizing functional

nanocomposite oxides with customizable structures and functionalities. First, since exsolution is a partial decomposition process, it can generate multiple phases[34] and different types of lattice defects[35-37] in the host oxides. Such defects are paramount for a wide range of electrical, optical and magnetic properties[38-40], which provides a tuning knob to tailor materials' functionality by controlling the extent of exsolution. Second, since exsolution can be implemented to a wide class of materials and does not require a delicate synthetic platform, it can act as a scalable and practical approach to synthesize self-assembled functional nanocomposites. For rational synthesis of exsolved nanocomposites, one has to carefully control the exsolution parameters through the underlying mechanisms. To date, it still remains unclear as to how exsolution affects the structure, chemistry and properties in the bulk of the host oxide.

In this work, we chose single-phase thin-film $La_{0.6}Sr_{0.4}FeO_3$ (LSF) as a model perovskite oxide to systematically investigate the bulk exsolution process. LSF is a suitable model system due to its well-studied bulk defect chemistry[41], and its broad applications in chemical looping[42], solid oxide cells[30] and magnetic nanostructure formation[43]. Moreover, thin-film LSF has also been employed as model systems to investigate surface exsolution in the previous studies.[30,37,44] We showed that exsolution in such oxide thin films generates not only metal nanoparticles (as in prior work), but also more complex nanostructures with implications for the thin-film properties; including crystalline Ruddlesden-Popper domains and percolated Fe-deficient nm-scale channels. These phenomena, to the best of our knowledge, are reported for the first time in LSF. While previous studies mainly focused on the exsolved metal nanoparticles, in this study we provide novel findings that the exsolution-induced extended defects can also be critical in determining the final functionality and property of the evolving composite material. Combining multimodal experiments with numerical simulations, we demonstrated that besides the exsolved Fe^0

nanoparticles, the Fe-deficient percolating channels formed during exsolution can increase the electronic conductivity of the nanocomposite LSF by more than two orders of magnitude.

Furthermore, we achieved a multi-state control of the exsolved nanocomposite and the quantification of that state reliably. For this, one needs to control the exsolution extent in the material and quantify its properties without altering the exsolution state. This task, however, is not trivial. In our previous study[37], we have shown that the surface exsolved metal nanoparticle can be quickly re-oxidized into metal oxides upon air exposure. Moreover, we have shown that the nanoparticle exsolution in thin film samples would not induce noticeable changes in the *ex-situ* XRD diffractions[37]. Therefore, it is very challenging, if not impossible, to accurately measure the exsolution states and the corresponding materials properties in the exsolved nanocomposites using *ex-situ* characterizations. To address this challenge, here we employed state-of-the-art near ambient pressure X-ray photoelectron spectroscopy (NAP-XPS) measurements to synthesize exsolved nanocomposite at different exsolution extents and at different stages of re-oxidation. Using this method, we unambiguously demonstrate that one can realize a multi-stage control of the electrical conductivity (by more than 2 orders of magnitude), and the magnetization (between 0 and 110 emu/cm^3) of the nanocomposite LSF by controllably tailoring the oxygen non-stoichiometry and the exsolution extent. These findings not only extend the mechanistic understanding on the bulk exsolution process, but also provide motivation to nano-engineer oxide thin films for novel and tunable properties *via* the exsolution route.

RESULTS AND DISCUSSION

Structure and chemistry of the exsolved nanocomposite LSF. To begin with, we demonstrate that bulk exsolution can transform a single-phase perovskite oxide into a metal/oxide nanocomposite (schematically shown in **Figure 1**a). In particular, we will examine the resulting heterogeneous chemical, atomic and electronic structure of the exsolved nanocomposite, as this has significant implications for the properties of interest. As shown in **Figure 1b**, 120 nm thick polycrystalline LSF films were deposited onto MgO (001) single crystal substrates using pulsed laser deposition (for film growth details see Methods). θ-2θ X-ray diffraction confirmed the dominant (001) texture of the polycrystalline LSF film, while a small amount of (011) contribution can also be observed (Supplementary Note 1). Scanning transmission electron microscopy (STEM) high-angle annular dark field (HAADF) imaging was employed to demonstrate the cross-sectional structure of the LSF films before and after exsolution. The as-prepared LSF specimen shows a columnar structure with little contrast other than vertical striations. After reducing the sample at 400 °C in 0.5 Torr flowing H_2, a variety of nanostructures with varying Z-contrast can be observed throughout the exsolved LSF film (**Figure 1**b). As shown in **Figure 1**c, nanoparticles can be clearly seen both on the surface and in the bulk of the exsolved sample. In accordance with the STEM images, the surface morphology of the LSF film also evolved during the exsolution process. After exsolution, small particles with a mean radius of ca. 8 nm appeared on the surface. Representative atomic force microscopy (AFM) and scanning electron microscopy (SEM) images are presented in the Supplementary Note 1.

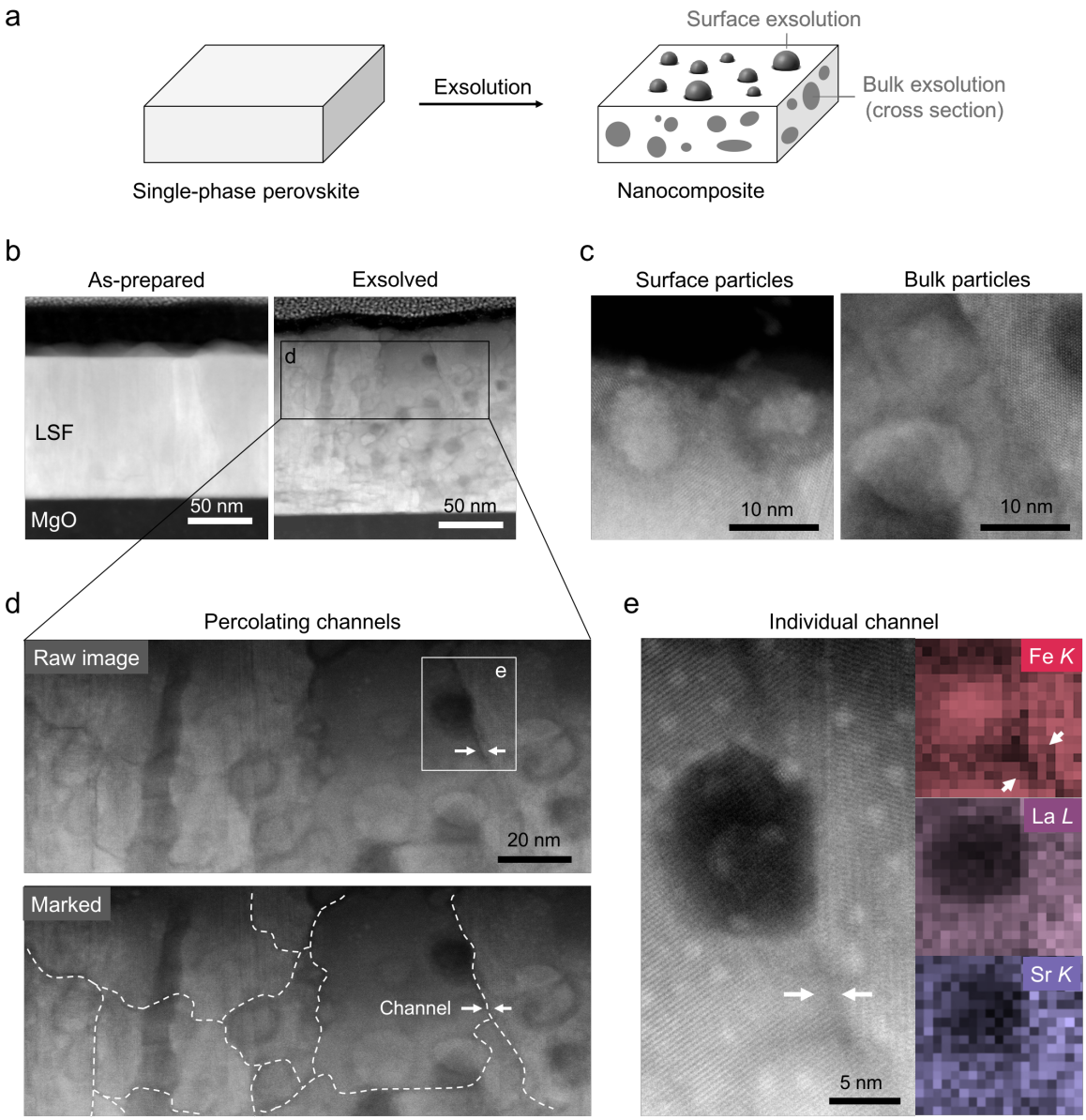

Figure 1. Exsolution nanocomposite. **(a)** Simplified sketch of synthesizing metal oxide nanocomposite *via* exsolution. (**b**) Cross-sectional scanning HAADF images of the LSF film before and after Fe^0 exsolution. **(c)** High resolution HAADF images showing the nanoparticles on the surface and in the bulk of the exsolved LSF film. (**d**) Magnified HAADF image from the region highlighted in (b) showing the percolating channels in the exsolved LSF film. The dashed lines marked the location of the channels. (**e**) High magnification HAADF and the corresponding EDX chemical mapping showing an individual channel. Note the channel is depleted in Fe. Plot (e) was collected from the region highlighted in (d) with a solid box.

Furthermore, we have also observed numerous channel-like features in the exsolved LSF film, featured by the threading dark stripes in **Figure 1**d-top. The nanoparticle precipitates are typically

located along these channels. As highlighted by the white dashed lines in **Figure 1**d-bottom, these channels form long-range connectivity (i.e., percolation[41]) across the entire exsolved sample. Since such percolating channels did not exist in the as-prepared sample (**Figure 1**b and Supplementary Note 1), they must be formed during the exsolution process together with the nanoparticles. The dark contrast of the percolating channels in the HAADF images suggest that they may contain considerable structural disorder[42]. In addition, these percolating channels are depleted in Fe as seen by energy dispersive spectroscopy (EDX) mapping (**Figure 1**e and Supplementary Note 2). We are aware that similar percolating channels have also been observed in partially decomposed cobalt-based perovskites[34] and lithium-excess cathode materials[43], and were identified as the fast cation migration channels in those systems. In analogy to those systems, the percolating channels in the exsolved LSF may act as the diffusion pathways that connects to regions where Fe has been exsolved from. This may also explain why the exsolved nanoparticles are preferentially located along these channels. It should also be noted that while each percolating channel appeared as a 1D line defect in the projected HAADF images (**Figure 1**d,e), they can be 2D structures in the interior of the film. In the following paragraphs, we will demonstrate that many of these channels are phase boundaries. At this point we cannot identify precisely the atomic and chemical state of these Fe-deficient percolating channels. For the remaining of the paper, we will refer to these features as "channels" for simplicity. The formation of such percolating structures is important to note because this can lead to significant changes in the macroscopic transport properties of the oxide film, arising from the local properties of these structures being different from those of the original material[43-45]. In this study, we will demonstrate that the exsolution-induced percolating channels can lead to an electrical conductivity increase by more than two orders of magnitude compared to the original LSF films (to be discussed later).

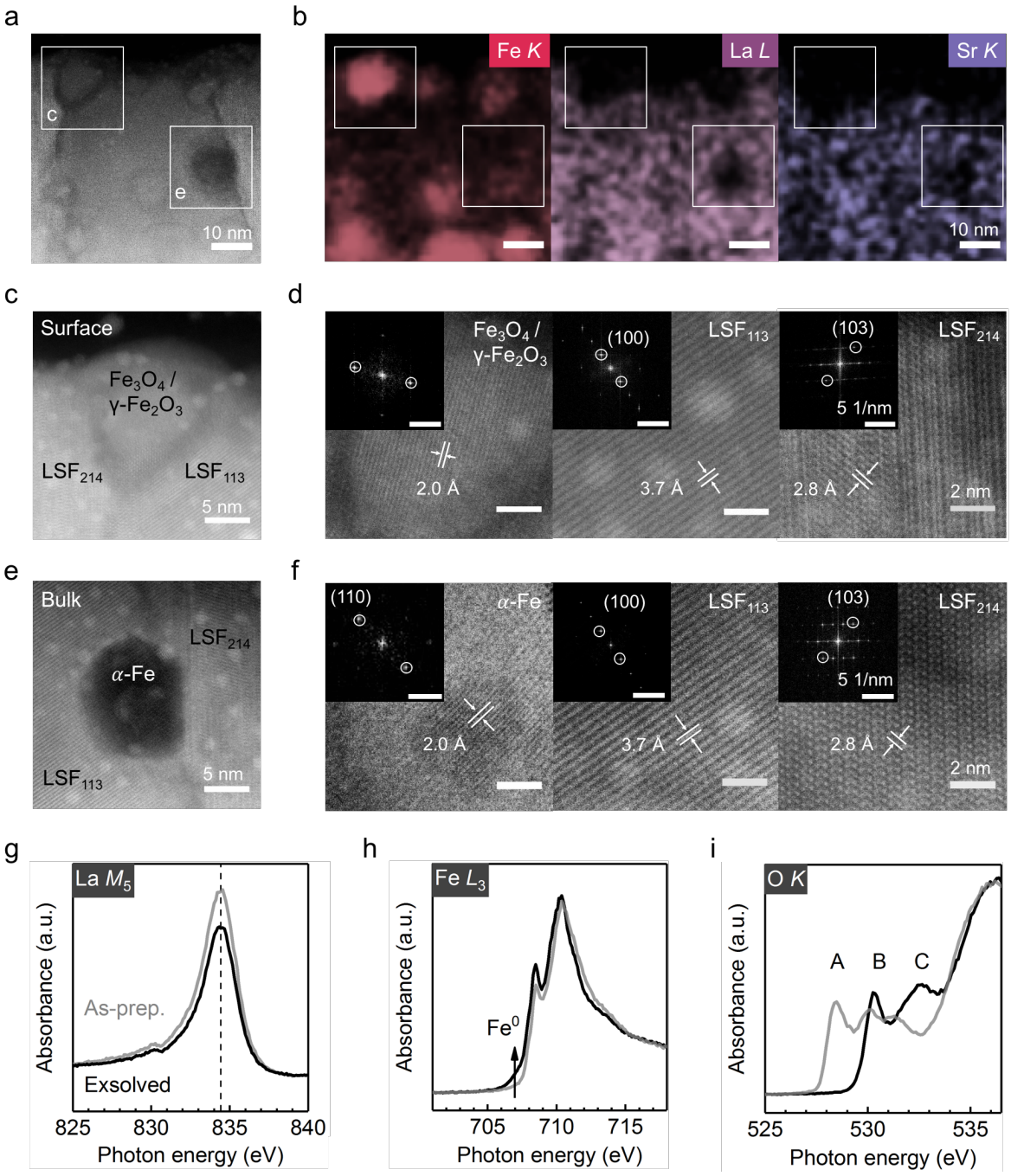

Figure 2. Atomic structure and chemical nature of the nanocomposite LSF. (**a**) Low magnification HAADF and (**b**) the corresponding EDX chemical mapping showing the chemical inhomogeneity of the exsolved LSF. High resolution HAADF images of the (**c**) surface and (**e**) bulk nanocomposite, which are acquired from the regions highlighted in (a,b) with the solid boxes. (**d, f**) High resolution images (scale bars: 2nm) showing the lattice fringes of the three different phases in (c, e) with the inset diffractogram from FFT (scale bars: 5 1/nm). The labeled lattice spacing corresponds to the circled FFT patterns. LSF_{113} and LSF_{214} denote the perovskite phase and the Ruddlesden-Popper phase, respectively. **(g)** La M_5-edge, (**h**) Fe L_3-edge, and (**i**) O K-edge PFY-XAS measurements revealing the macroscopically averaged bulk chemistry and electronic structure of the LSF film before (gray lines) and after (black lines) exsolution.

A detailed phase analysis of the exsolved nanocomposite LSF is presented in **Figure 2**. Unlike the as-prepared LSF film that has a homogeneous bulk chemistry (Supplementary Note 3), the exsolved LSF exhibited considerable chemical inhomogeneity. As shown in **Figure 2**a,b and **Figure** S8, the nanoparticles both at the surface and in the bulk are enriched in Fe while depleted in La and Sr. Zoom-in views of these Fe-enriched nanoparticles are presented in **Figure 2**c,e. With the aid of fast Fourier transformation (FFT) analysis (**Figure 2**d,f), we assign the bulk nanoparticles to be α-Fe (PDF#00-006-0696[46]). Meanwhile, surface nanoparticles could be either Fe_3O_4 (PDF#01-071-6336[47]) or γ-Fe_2O_3 (PDF# 00-039-1346[48]). As both iron oxide phases adopt similar inverse spinel structures[49,50], we cannot unambiguously distinguish between them in this work. Nevertheless, the observation of iron oxides on the surface clearly indicates that the surface Fe^0 particles became oxidized during sample transfer for TEM analysis. In agreement with our findings, re-oxidation of the surface exsolved metal nanoparticles into metal oxides has also been reported in previous studies[30,51]. On the other hand, the α-Fe particles embedded in the bulk are protected from oxidation upon air exposure of the sample surface.

The fuzzy layer around the exsolved nanoparticles reflects the phase boundary. As labeled in **Figure 2**c,e, we identified two distinct phases adjacent to the exsolved nanoparticles. Based on the interatomic lattice spacing revealed by the high resolution images (**Figure 2**d,f), we assigned these two phases to be perovskite-type (La,Sr)FeO_3 (PDF#04-007-6521[52]) and Ruddlesden-Popper-type $(La,Sr)_2FeO_4$ (PDF#01-082-8811[53]), and denoted as LSC_{113} and LSC_{214} respectively. These observations indicate that many of Fe-deficient percolating channels observed in **Figure 1**d,e are phase boundaries between the LSF_{113} and LSF_{214} domains. Nevertheless, as shown in the Supplementary Note 2, we also find a few percolating channels are located within a single phase.

Therefore, the Fe^0 nanoparticle exsolution both at the surface and in the bulk is correlated with the formation of the Ruddlesden-Popper (RP) phase. This is consistent with the bulk phase decomposition of LSF into iron metal and RP phase under reducing conditions[54,55]. As such, we can describe the nanocomposite formation in LSF with the following reaction:

$$2(\mathrm{La,Sr})\mathrm{FeO}_{3-\delta} \rightarrow (\mathrm{La,Sr})_2\mathrm{FeO}_{4-\delta'} + \mathrm{Fe}^0 + (2+\delta'-2\delta)\mathrm{O}_{\mathrm{atm}}, \quad (1)$$

where $\mathrm{O}_{\mathrm{atm}}$ denotes a gas-phase oxygen, which can be present in the form of different molecules (such as H_2O or CO_2) depending on the reducing agent. Meanwhile, δ and δ' denote oxygen nonstoichiometry in the perovskite and RP phase, respectively. We are aware that cation vacancies can also exist in both phases. Nevertheless, since the purpose of Eq. 1 is to provide a general description of the exsolution process, we use the current format for simplicity. It should be also noted that we did not observe discernible reflections from the α-Fe and RP phases in the nanocomposite LSF with θ-2θ XRD (Supplementary Note 1), likely due to the small crystalline volume fraction of both phases. Therefore, we expect the perovskite LSF remains as the dominant phase (matrix) even after Fe^0 exsolution. The preservation of the perovskite-type structure indicates a good structural stability of the LSF lattice during Fe^0 exsolution under the conditions of these experiments.

Finally, we employed *ex-situ* partial fluorescence-yield X-ray absorption spectroscopy (PFY-XAS) to demonstrate the evolution of bulk chemistry upon nanocomposite formation. For La M_4-edge (**Figure 2**g), we did not observe noticeable changes in the main peak, indicating a constant oxidation state of La during exsolution. On the other hand, the increased pre-edge intensity at ca. 707 eV in Fe L_3-edge after exsolution (**Figure 2**h) suggests the presence of metallic iron (Fe^0) in the nanocomposite LSF[56]. Note the Fe^0 feature in the Fe L_3-edge agrees well with the α-Fe particles

observed by STEM characterization (**Figure 2**e,f). Regarding the O *K*-edge (**Figure 2**i), the pre-edge feature A in the as-prepared LSF corresponds to the transition from O 1*s* to the ligand hole $\underline{L}$ in the $3d^5\underline{L}$ configuration[57,58]. The pre-edge peak vanished after exsolution, indicating a filling of the ligand band, which corresponds to a reduction of the LSF film.[57]. In agreement with the pre-edge evolution in the O *K*-edge, lattice chemical expansion[59,60] has also been observed after exsolution (Supplementary Note 1), which confirms the increased oxygen vacancy concentration in the nanocomposite LSF. The two peaks between 529 and 532 eV (feature B) in the as-prepared LSF have been assigned to the unoccupied $t_{2g}\downarrow$ and $e_g\downarrow$ states, respectively[57,58]. The variation of these absorption features during exsolution may indicate a change in covalency[57]. Finally, a new feature emerged at around 532.5 eV (feature C) after exsolution. Since feature C did not exist in the mildly reduced LSF film (Supplementary Note 4), it should be related to the new phase(s) or lattice defect(s) that are formed in exsolution. Accordingly, the peak position of feature C agrees with the La/Sr-O hybridization of La_2O_3[61], SrO[61], and Ruddlesden-Popper (RP) phase oxides[34,62,63], which are all likely decomposition products of LSF during exsolution[19,64-66]. Therefore, while the nanocomposite LSF is mainly composed of the perovskite matrix, it exhibits completely different electronic structures from the perovskite LSF. As indicated earlier, this will have implications for the resulting electronic and magnetic properties of the exsolved nanocomposite with respect to the initial LSF.

Enhanced electrical conductivity from *in situ* Fe^0 exsolution

Having demonstrated that Fe^0 exsolution can transform the single-phase perovskite LSF into a triple-phase nanocomposite, we now turn to its impact on the functionalities of the material. The experimental setup is schematically shown in **Figure 3**a. As illustrated, NAP-XPS and in-plane electrical conductivity measurements were performed simultaneously to monitor the surface and bulk properties of the LSF film *in-situ* at different stages of Fe^0 exsolution.

The typical O 1*s* and Fe 3*p* spectra of the LSF film during Fe^0 exsolution are presented in **Figure 3**b. We deconvoluted the Fe 3*p* spectra into two components: one metallic (Fe^0) species at low binding energy and one oxidized iron species (Fe^{2+} and/or Fe^{3+}) at high binding energy[67]. We are aware that the peak model is a simplification of the complex Fe peak structure. Nevertheless, utilizing these reduced fitting parameters allowed us to quantify the relative proportions of metallic and oxidized irons at the surface *in situ* in a facile way. For the O 1*s* spectra, we identified a total of three oxygen species. The highest binding energy species (denoted as O_{Surf}) is typically assigned to a SrO segregation layer at the surface of the perovskite[68]. Since the O_{Surf} component only exists before Fe^0 exsolution and irreversibly disappeared after heating in H_2, we will not discuss it further in this paper. The most intense peak (denoted as O^{2-}) that exists in all the experimental conditions is assigned to the lattice oxygen atoms from the perovskite and/or RP phases[69-71]. The shoulder feature (denoted as O^*) at ~ 1.1 eV higher binding energy than the O^{2-} species only appeared after the onset of exsolution and did not vanish even after Ar^+ sputtering under ultra-high vacuum conditions (Supplementary Note 5). Therefore, the O^* feature should not originate from surface adsorbates[72]. Instead, we expect the O^* species to be associated with the non-stoichiometric defect regions that were formed during Fe^0 exsolution. Based on the STEM characterizations presented in the previous section, one such defect region can be the phase boundaries between the metallic

iron, RP phase, and the perovskite lattice. While further investigations are required to elucidate the exact chemical nature of the O^* species, its concentration *indirectly* measures the extent of surface decomposition in LSF during Fe^0 exsolution. As will be shown below, the temporal changes in the intensities of Fe^0 and O^* are consistent with each other, which validates our assignment.

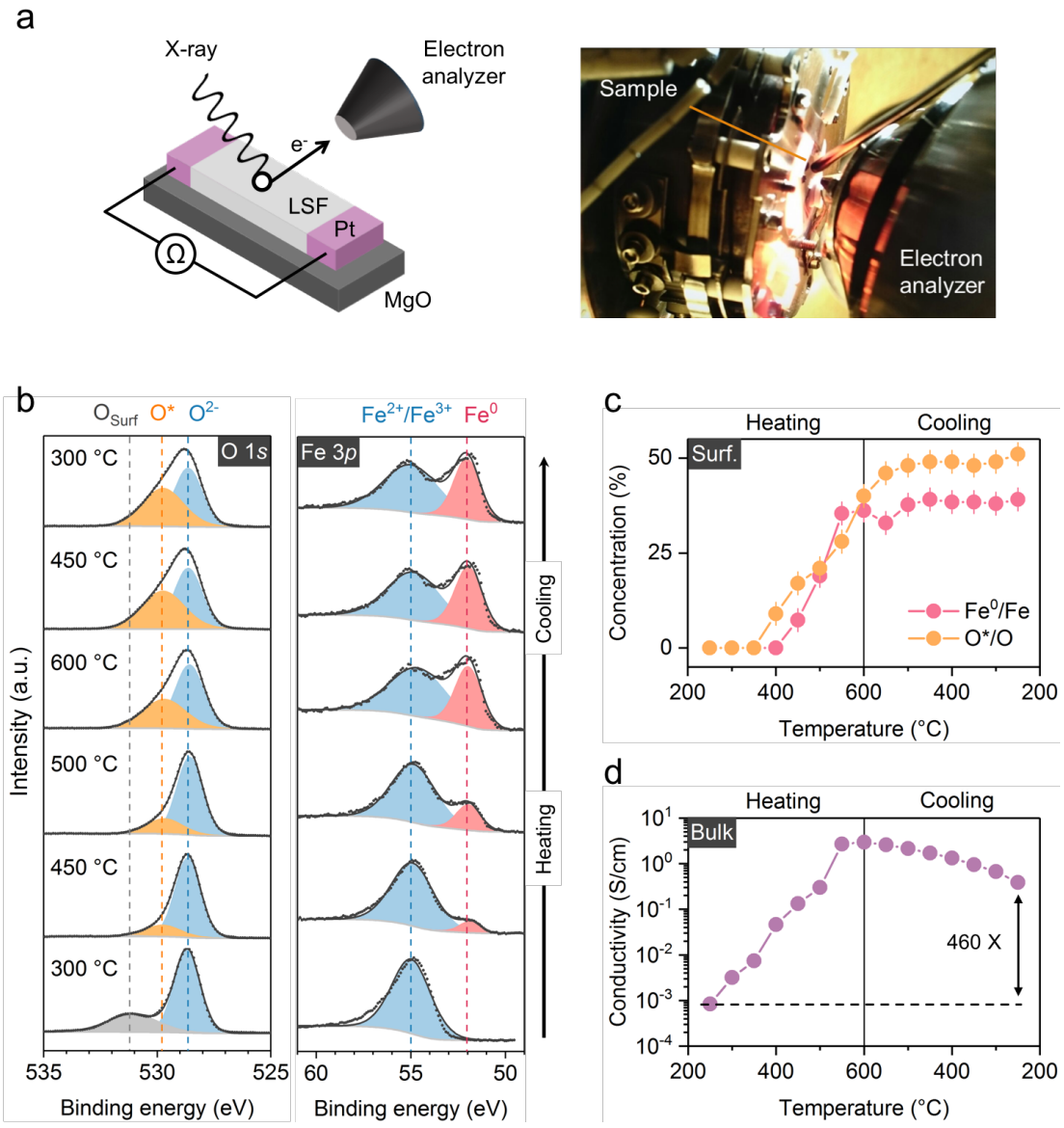

Figure 3. Evolution of surface chemistry and electrical conductivity of LSF upon nanocomposite formation. (**a**) Schematics and photo image of the experimental setup. (**b**) Fe 3*p* and O 1*s* NAP-XPS spectra and (**c**) the quantified surface concentrations of Fe^0 and O^* at the LSF surface during heating and cooling in 0.5 Torr H_2. Origins of each surface species are described in the main text. (**d**) In-plane electrical conductivity of the LSF films during heating and cooling in 0.5 Torr H_2. Note the Fe^0 exsolution clearly alters both the surface and bulk properties of the LSF.

Therefore, we can use the surface concentrations of Fe^0 and O^* to quantitatively determine the extent of exsolution in LSF (**Figure 3**c). During the heating step, the normalized O 1s intensity gradually decreased (Figure S15), which indicates oxygen vacancy formation (i.e., lattice reduction)[37]. The Fe^0 species appeared on the surface at 450 °C, which marked the onset of Fe^0 exsolution. Upon further heating in 0.5 Torr H_2, the surface concentrations of Fe^0 and O^* increased synergistically with temperature, indicating an increasing extent of Fe^0 exsolution in the LSF film. The correlation between the surface concentrations of Fe^0 and O^* further supports our assignment that the O^* species are the side products of Fe^0 exsolution. During the cooling step, the LSF film cannot exchange oxygen with the atmosphere as there is no oxygen source in the chamber[73]. As a result, the LSF surface maintained a constant stoichiometry during the cooling step, which is exemplified by the invariant Fe^0 and O^* concentration (**Figure 3**c) and the stable O 1*s* intensity (Figure S15). Cooling in H_2 atmosphere thus enables the preservation of the nanocomposite LSF.

Simultaneously with the NAP-XPS measurement, the in-plane DC electrical conductivity of the LSF films was characterized. As shown in **Figure 3**d, the in-plane electrical conductivity of the film exhibited an asymmetric temperature dependence during respective heating and cooling steps. In particular, the electrical conductivity of the LSF film increased significantly after being heated in H_2 (i.e., after Fe^0 exsolution). As an example, the in-plane conductivity of the LSF film increased by ca. 460 times at 250 °C after Fe^0 exsolution. The appearance of surface Fe^0 and O^*, together with the enhancement in electrical conductivity, clearly demonstrated that Fe^0 exsolution can profoundly modulate the bulk properties of the LSF film. Moreover, the observed increase in surface Fe^0 concentration as well as bulk electrical conductivity (upon nanocomposite formation) are beneficial in improving the electrochemical performance of the materials[74-76].

Tunable electronic transport in the nanocomposite LSF

In this section, we show the enhanced electrical conductivity in the nanocomposite LSF is mainly electronic, highly tunable and arises from the Fe-deficient percolating channels. To do so, we prepared LSF films at three different stages of Fe^0 exsolution: prior to, after medium, and after heavy Fe^0 exsolution. The extent of Fe^0 exsolution in each sample was controlled by monitoring the surface chemistry with NAP-XPS during thermal reduction in 0.5 Torr H_2. As illustrated in **Figure 4**a, the LSF sample with the most intense Fe^0 exsolution is featured by the highest surface concentrations of Fe^0 and O^*. The "no exsolution" state in **Figure 4** corresponds to the LSF film reduced in 0.5 Torr H_2 at 400 °C, where no Fe^0 can be observed with NAP-XPS (**Figure 3**c). For each sample, we characterized its electrical conductivity right after sample synthesis in 0.5 Torr H_2, without air exposure, in the cooling direction. As the electrical conductivity was measured in the cooling direction, the exsolution states in the sample were kinetically trapped. The kinetically trapped exsolution state can be inferred by the stable surface defect chemistry and oxygen non-stoichiometry during the entire conductivity measurement (**Figure 3**c and Figure S15). As such, we can directly compare the intrinsic electrical properties of the nanocomposite LSF at different exsolution states. All the conductivity data were obtained after annealing the sample at the highest reduction temperature for ~ 0.5 hour (see Methods). Longer reduction time, however, may result in more exsolved (decomposed) states. Therefore, the conductivity data reported in this study should represent snapshots of certain exsolution states that are defined by *both* the annealing temperature and time.

The temperature-dependent electrical conductivities (σT) of the nanocomposite LSF films in 0.5 Torr H_2 and in the cooling direction are summarized in **Figure 4**b. As illustrated, the total electrical conductivity of the LSF film progressively, and substantially increased with the increasing extent of Fe^0 exsolution. As an example, the electrical conductivity of the LSF film increased by more

than two orders of magnitude at 400 °C after exsolution. The extent of electrical enhancement was even larger at lower temperatures. In particular, the electrical conductivities for the LSF films at different stages of exsolution all exhibit a temperature-activated, Arrhenius-type behavior. This is interesting as it immediately indicates that the strong enhancement in electrical conductivity does not originate from the metallic phase. In the following paragraphs, we are going to show that the change in the total electrical conductivity mostly likely stems from the formation of the abovementioned percolating Fe-deficient channels in the nanocomposite LSF (see **Figure 1**).

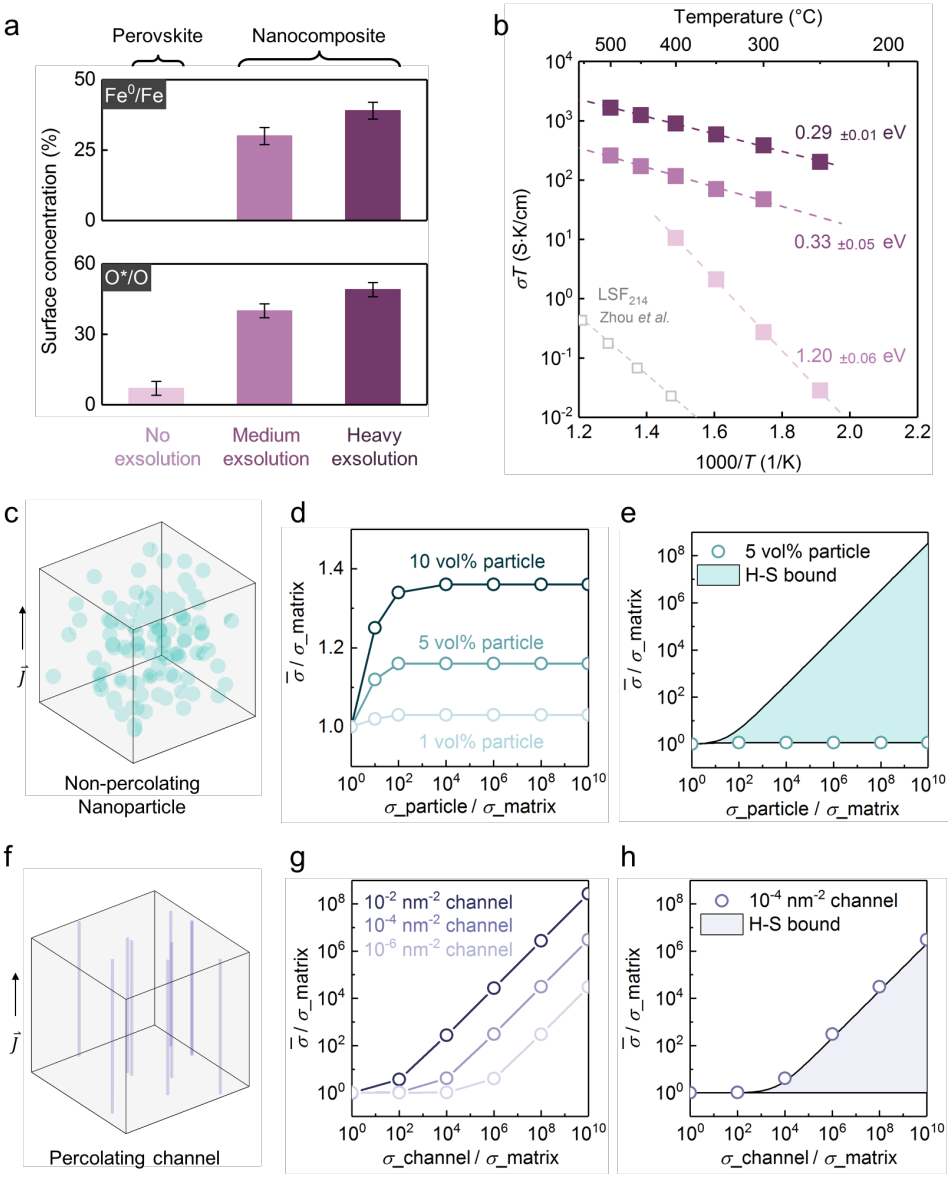

Figure 4. Electrical conductivity of nanocomposites. (a) Surface chemistry at three different exsolution stages: before exsolution, medium exsolution, and heavy exsolution (quantified with NAP-XPS). **(b)** In-plane electrical conductivities of the same samples as in (a), where the dashed lines represent the best fit to the Arrhenius relation (see Supplementary Note 7). The conductivities were measured in the cooling direction in 0.5 Torr H_2 and the activation energies are presented with 95% confidence interval. The color codes in (b) are the same as in (a). The electrical conductivities of the RP phase $La_{1.2}Sr_{0.8}FeO_4$ (denoted as "LSF_{214}") in 5% H_2/Ar atmosphere[77] are also shown for comparison. (**c-h**) Finite element analysis (FEA) of the contributions from the non-percolating nanoparticles and percolation channels to the electrical conductivity enhancement. (**c, f**) FEA models. (**d, g**) Electrical conductivity of the nanocomposite as a function of (d) nanoparticle density, and (g) channel density. (**e, h**) Comparison of the finite element calculation to the Hashin–Shtrikman (H-S) bounds. Note the percolating channels are more effective in increasing the total electrical conductivity than the non-percolating nanoparticles.

To resolve the mechanism of enhanced conductivity, we first analyze the evolution in activation energies. As shown in **Figure 4**b, the reduced perovskite LSF (prior to exsolution) had poor conductivity in H_2 with an activation energy of 1.2 eV. The measured activation energy agrees well with previous studies on the bulk LSF in reducing atmospheres[78]. The high activation energy suggests that the ionic contribution is significant in the total conductivity, which originates from the minimal concentrations of electrons and holes in the reduced LSF. A detailed defect chemistry and conductivity analysis is presented in the Supplementary Note 6. After Fe^0 exsolution, the activation energy decreased from 1.2 eV to ~0.3 eV for both the medium- and heavily-exsolved LSF films. The low activation energies indicate that the electronic conduction dominates the nanocomposite LSF, which was further supported by the impedance characterization (Supplementary Note 7). Therefore, based on the activation energy and impedance analysis, we confirmed that the electronic contributions dominate the total conductivity in the nanocomposite LSF. In other words, in the experimental conditions of this work, Fe exsolution turns LSF from a dominantly ionic conductor and electronic insulator, to a dominantly electronic conductor. When varying the extent of exsolution in a nanocomposite LSF, above the limit where a new conduction mechanism dominates, one tailors the concentration of charge carriers. That means the conduction mechanism remains the same for the medium and heavily exsolved LSF films, evident from their identical activation energies.

We then assess the different components of the exsolved LSF and demonstrate that the enhanced electronic conductivities should originate from the percolating channels. First of all, we show that the conductivity enhancement does not originate from the LSF_{113} perovskite phase. As illustrated above (**Figure 4**b and Supplementary Note 7) and also in other studies[35,36], the perovskite matrix became off-stoichiometric during the exsolution process. Such off-stoichiometry in the LSF matrix

can strongly decrease its electronic conductivity. This is because the electronic conduction in the LSF lattice occurs along Fe-O-Fe chains,[79,80] and a disruption of these chains by introduction of oxygen and Fe vacancies would impede the hopping of the electronic charge carriers[81]. In support of this model, both oxygen and B-site vacancy formation were found to lower the electrical conductivity in LSF[81] and other perovskite systems.[40,82]

Second, we show that the formation of RP-type LSF_{214} during exsolution does not explain the observed conductivity enhancement. As shown in **Figure 2**, we observed RP phase formation in the bulk lattice during Fe^0 exsolution. To assess the effect of the RP phase formation on the total conductivity change, we plotted the conductivity of the $La_{1.2}Sr_{0.8}FeO_4$ in **Figure 4**b (data from ref. [77], measured in 5% H_2/Ar gas atmosphere). As illustrated, $La_{1.2}Sr_{0.8}FeO_4$ exhibited a much lower electrical conductivity than the perovskite phase LSF in H_2 atmosphere. Consequently, we expect the formation of only RP phase as a by-product to Fe^0 exsolution would rather decrease the total electrical conductivity of the film instead of increasing it.

Thirdly, we show that the formation of the exsolved Fe^0 nanoparticles cannot explain the conductivity enhancement, either, because they are not percolated as seen in the STEM images in **Figure 1**. For this, we conducted finite element analysis (FEA) to calculate how the total conductivity is affected by the conductivity and density of the exsolved nanoparticles. As shown in **Figure 4**c, the nanoparticles were modeled as homogeneously dispersed spheres of 5 nm radius (see Methods for the detailed modeling description). According to the magnetic measurement, the total volume fraction of the Fe^0 nanoparticles in the exsolved LSF film was around 6% (Supplementary Note 8). Therefore, we varied the volume concentrations of the spheres between 0 and 10% in the FEA modeling and the results are displayed in **Figure 4**d. For better visualization, we normalized the particle conductivity ($\sigma_{\mathrm{particle}}$) and the spatially averaged total conductivity ($\bar{\sigma}$)

to that of the LSF matrix (σ_{matrix}). As shown in **Figure 4**d, introduction of non-percolating nanoparticles to the matrix has minimal impact on the total conductivity. By increasing the particle conductivities ($\sigma_{\mathrm{particle}}/\sigma_{\mathrm{matrix}}$) from 10^0 to 10^{10}, the total conductivity of the nanocomposite ($\bar{\sigma}/\sigma_{\mathrm{matrix}}$) can only increase up to 40%. Therefore, the non-percolating nanoparticles cannot explain the more than 100 times higher electrical conductivity observed in **Figure 3**d.

Finally, we show that the percolating channels can substantially modulate the total electrical conductivity of the exsolved LSF film. As shown in **Figure 1**d, Fe^0 exsolution forms both in-plane and cross-plane percolating channels in the LSF matrix. Since the channels that are perpendicular to the electrical current have negligible impact on the total electrical conductivity (Supplementary Note 9), we focus on the channels that percolate in the same direction as the electrical currents (i.e., the in-plane direction). While the channels can be 2D shapes traversing the matrix, we modeled the channels as cylinders oriented parallel to the electrical current for computational efficiency (**Figure 4**f). Based on the STEM characterizations (**Figure 1**e), we set the cylinder radius to be 1 nm and varied the cylinder densities (i.e., the total channel length per unit volume) between 10^{-6} to 10^{-2} cm^{-2} in the model. As shown in **Figure 4**g, we find the total conductivity ($\bar{\sigma}/\sigma_{\mathrm{matrix}}$) increased significantly with the channel conductivity ($\sigma_{\mathrm{channel}}/\sigma_{\mathrm{matrix}}$), evident from the logarithmic scale in the plot. To further elucidate the role of percolating channels in modulating the total conductivity, we compared our modeling to the theoretical Hashin-Shtrikman (H-S) bounds[83]. As indicated by the shaded regions in **Figure 4**e and **Figure 4**h, the H-S bounds provide theoretical bounds for the macroscopic electrical conductivity of isotropic two-phase media of

arbitrary phase geometry. As illustrated, the non-percolating nanoparticles and percolating channels essentially represent the upper and lower H-S bounds, respectively.

Based on these results, we expect the electronic conductivity enhancement in the nanocomposite LSF can only originate from the formation of percolating channels. Several factors could contribute to the observed enhanced electronic conductivities. First, as revealed by the EDX mapping (**Figure 1**e) and XPS analysis (**Figure 3**c and Supplementary Note 10), the percolating channels can be highly off-stoichiometric and contain high concentrations of lattice defects. Due to charge neutrality, the off-stoichiometry and lattice defects in the percolating channels may lead to locally enriched electronic charge carriers, which can result in an apparent higher electronic conductivity. Second, the observed electronic conductivity enhancement may also originate from interface effects. As discussed in **Figure 1** and **Figure 2**, many of the percolating channels are located near the phase boundaries. Such heterostructures may also lead to emergent transport properties[6-9]. For example, Chang *et al*. observed a confined polaronic transport near the $LaFeO_3/SrFeO_3$ interface, which results in a significantly enhanced electronic conductivity as well as a reduction in the activation energy[84]. Previous studies have also demonstrated that the space-charge layer near the extended defects can significantly modulate the total electronic conductivities of the oxides[39,85,86]. While further studies are needed to elucidate the detailed conduction mechanisms, our results unambiguously demonstrate that Fe^0 exsolution can be used as an effective tuning parameter to tailor the electronic conductivities of the nanocomposite LSF.

Tuning nanocomposite magnetism *via* redox switching

As seen in recent exciting studies, oxygen non-stoichiometry in oxides can be utilized to control the materials' magnetic properties[87-89]. Motivated by this idea, we demonstrate in this section that one can further modulate the magnetism of the nanocomposite LSF *via* reversible redox switching of the precipitated Fe nanoparticles. To examine the redox behavior of the nanocomposite LSF, we cycled the exsolved LSF film between 0.2 Torr O_2 and 0.5 Torr H_2 at 400 °C (for experimental details, see Supplementary Note 10). The temperature is chosen to be below the exsolution onset (450 °C, see **Figure 3**) so that no additional exsolution would occur from the host oxide.

The *in-situ* NAP-XPS analysis of the nanocomposite LSF during the redox cycles are summarized in **Figure 5**a-c. First, after each oxidation treatment, the Fe^0 species disappeared and the O^* concentration decreased to ~10%. These findings indicate that the oxidative treatment not only oxidized the surface Fe^0 nanoparticles, but also partially recovered the surface defects that had been formed in exsolution. Second, after the successive reduction treatment, the Fe^0 species appeared again on the surface, together with an increase in the O^* concentration. Since the reduction temperature is below the exsolution onset, no further Fe^0 exsolution should occur. Therefore, the resurgence of Fe^0 and O^* indicates that the surface Fe^0 nanoparticles did not reintegrate into the host oxide upon re-oxidation, but were oxidized to iron oxides. *Ex-situ* AFM measurements also confirmed that the nanoparticles did not dissolve upon re-oxidation (Supplementary Note 10). This is reasonable because the exsolved nanoparticles would only dissolve at very high temperatures.[19,26-28] On the other hand, mild oxidation would only oxidize the Fe^0 nanoparticles into iron oxides[30]. Then, the successive reduction process reduced these iron oxides back to Fe^0 and (partially) regenerated the surface defects (i.e., the O^* species). As the reduction temperature (400 °C) is lower than that of the exsolution condition (600 °C, see **Figure**

3), the surface concentrations of Fe^0 and O^* after the re-reduction step were smaller than that of the as-exsolved LSF surface (cycle 0).

Therefore, **Figure 5**a-c unambiguously demonstrate that both the surface exsolved iron nanoparticles (featured by the surface Fe^0 species) and the surface oxide lattice (featured by surface O^*) can reversibly exchange oxygen with the gas atmosphere even at temperatures below the exsolution onset. As stated in the Introduction section, the unique redox capability to cycle exsolved Fe nanoparticles between the metallic and oxide states is crucial in both catalytic activity switching[30] as well as catalyst regeneration[19,31]. The highly reversible surface chemistry during the redox cycling also highlights the redox stability of the nanocomposite LSF film.

Having demonstrated the reversible surface redox capability, we then turn to the bulk redox properties of the nanocomposite LSF. To probe the phase evolution of the embedded nanoparticles, we employed magnetic measurements due to their exceptional sensitivity to the ferromagnetic exsolved nanoparticles[90,91]. As metallic iron has much higher magnetization than the iron oxides, oxidation of the embedded Fe^0 nanoparticles should result in a decreased saturation magnetization[92,93]. Therefore, the saturation magnetization of the LSF nanocomposite can be used to estimate the oxidation state of the exsolved nanoparticles. We employed vibrating-sample magnetometry (VSM) to probe the magnetic property of the nanocomposite LSF at different stages of the redox cycling: as-exsolved, mildly oxidized, and heavily oxidized. The surface chemistry of each sample before taking out of the XPS chamber is shown in **Figure 5**d.

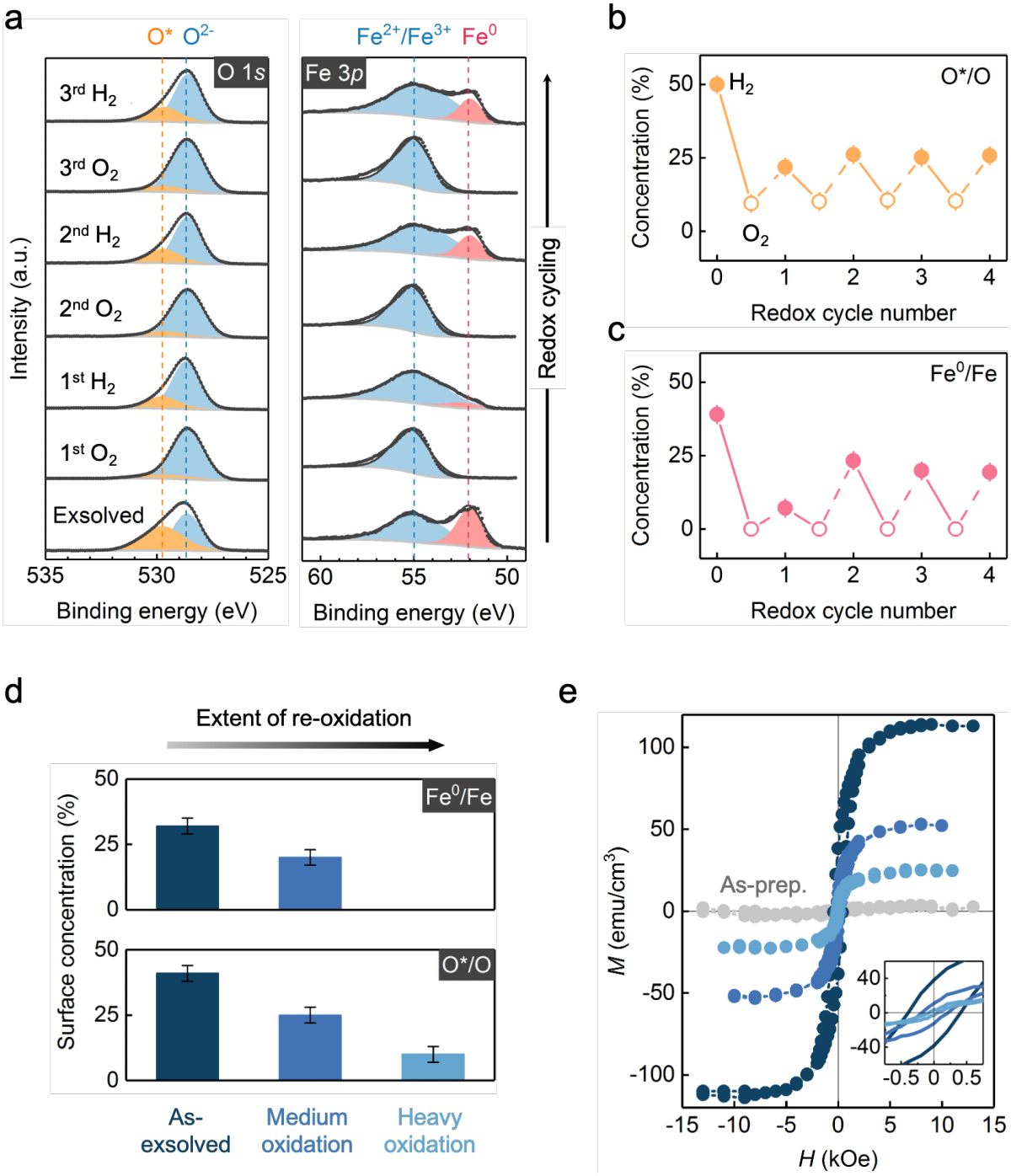

Figure 5. Redox properties of the nanocomposite LSF. (a) NAP-XPS Fe 3*p* and O 1*s* spectra, surface concentrations of (**b**) O^*, and (**c**) Fe^0 of the exsolved LSF film during redox cycling between 0.2 Torr O_2 (empty symbols) and 0.5 Torr H_2 (solid symbols) at 400 °C. The solid and dashed lines in plot (b) and (c) indicate the oxidation and reduction step, respectively. Here, cycle 0 represents the as-exsolved state. (**d**) *In-situ* surface chemistry quantified with NAP-XPS and (**e**) *ex-situ* room temperature magnetization vs field (*M–H)* loops of the LSF films at different stages of the redox cycling: as-exsolved, medium oxidized, and heavily oxidized. The color codes in (e) are the same as in (d). Meanwhile, the as-prepared LSF (without exsolution) is also shown in (e) for comparison. *M* is normalized to the total volume of the film. The inset figure in (e) highlights the decrease in coercivity upon re-oxidation.

Figure 5e summarizes the room-temperature in-plane magnetic hysteresis loops of these three samples, along with that of the as-prepared state. As illustrated, the as-prepared LSF film shows negligible magnetic hysteresis, which is consistent with the reported weak ferromagnetism in $La_{0.6}Sr_{0.4}FeO_3$ (Ref.[94]). After Fe^0 exsolution, however, magnetic hysteresis (M–H) loops are clearly present at room temperature with a saturation magnetization (M_S) of about 110 emu/cm^3 (normalized by the entire volume of LSF film). Since both the reduced perovskite LSF matrix (Supplementary Note 11) and the RP phase LSF_{214} (ref. [95]) have negligible magnetic properties, the enhanced magnetism is due to the formation of ferromagnetic exsolved nanoparticles. Since the embedded Fe^0 nanoparticles can maintain their metallic state even upon air exposure at room temperature (**Figure 2**), we expect the magnetism of the as-exsolved LSF to be mainly determined by the Fe^0 nanoparticles embedded within the LSF film. In accordance with the isotropic geometry and uniform spatial distribution of the exsolved Fe^0 nanoparticles (**Figure 1**), the nanocomposite LSF exhibited similar in-plane and out-of-plane magnetic properties (Supplementary Note 11). If the Fe nanoparticles have the bulk magnetization of iron, the net magnetization of the film implies 6% by volume of nanoparticles. The estimated volume fraction agrees well with the TEM observation, where the particle area fraction is ~8% (Supplementary Note 8).

The successive oxidation treatment progressively reduced the saturation magnetization to ~25 emu/cm^3. As the oxidation temperature is too low for the exsolved nanoparticles to reintegrate into the lattice (Supplementary Note 10), the decrease in the total saturation magnetization originates from the oxidation of the embedded Fe^0 nanoparticles into iron oxides. A likely scenario would be that the re-oxidation process occurred *via* the growth of oxide shells at the expense of Fe^0 cores, forming core-shell structures during the evolution of oxidation. A similar phenomenon has also been observed in the oxidation of iron nanoparticles[93]. In accord with this hypothesis, the coercivity

of the nanocomposite LSF also decreased upon re-oxidation (inset figure in **Figure 5**e). Since the embedded Fe^0 particles in the nanocomposite LSF adopt single-domain structures (Supplementary Note 8), a decrease in coercivity is consistent with a reduction in size of the Fe^0 core and in the thermal stability of the magnetization upon oxidation[96]. The continuous modulation of the saturation magnetization and coercivity of the nanocomposite LSF thus reflects the reversible oxidation of the embedded Fe^0 nanoparticles. Moreover, our observations demonstrate one can realize a multiple-state control of the nanocomposite LSF *via* oxygen non-stoichiometry. Note that the tuning range of the magnetic moment in the nanocomposite LSF (from zero to ~110 emu/cm^3) is comparable to other state-of-art perovskite systems[97]. Note that while we demonstrate here the modulation of magnetism modulation at elevated temperatures and slow rate, the switching could potentially be done at a much faster rate and at room temperature if we use electrochemistry to trigger the redox switching[30,97,98]. Therefore, redox switching can be an effective "tuning knob" to dynamically manipulate the microstructure, phase composition, and magnetic properties of the exsolved nanocomposite.

CONCLUSION

In summary, this study demonstrates a novel utility of exsolution in preparing nanostructured, multi-phase metal oxides with tunable properties. First, we showed that Fe^0 exsolution can induce a drastic chemical and structural reorganization both at the surface and in the bulk of LSF, transforming the single-phase perovskite into a multi-phase nanocomposite that consists of Fe^0 nanoparticles, crystalline Ruddlesden-Popper domains, and percolated Fe-deficient nm-scale channels. Second, by comparing nanocomposite LSF at different stages of Fe^0 exsolution, we demonstrated that the extent of Fe^0 exsolution can be used as an effective tool to tailor the chemical, electrical, and magnetic properties of the nanocomposite LSF. We found that, in addition to the

exsolved nanoparticles, the exsolution-induced lattice defects can profoundly impact the properties of the material. In particular, we observed an increase in the electronic conductivity by more than two orders of magnitude, turning LSF from a dominantly ionic conductor to a dominantly electronic conductor. With the aid of numerical analysis, we demonstrated that such large change in conductivity can only arise from the Fe-deficient percolating channels formed during exsolution in this structure. Moreover, as both the surface and the embedded exsolved Fe nanoparticles are highly redox active, the magnetic properties of the nanocomposite LSF can be modulated *via* redox control. At moderate temperatures even below the exsolution onset, we achieved a continuous control of the magnetic properties of the nanocomposite LSF between 0 to 110 emu/cm^3. Besides the temperature and gas atmospheres that are used in this work, other external stimuli such as electrochemical overpotential[30] and photo-illumination[99] could also be employed to tailor exsolution, and hence the geometry and functionalities of the resulting nanocomposite. Moreover, while this paper focused on the thin-film system, it is conceivable that one can also synthesize bulk versions of nanocomposite materials *via* exsolution. The findings of this work thus highlight the potential of bulk exsolution in synthesizing tunable multifunctional nanocomposites, which can benefit a broad range of applications including solid oxide cells, nanophotonics, thermoelectric devices, multiferroics, and memory/logic technologies.

METHODS

Sample preparation: The thin-film $La_{0.6}Sr_{0.4}FeO_3$ (LSF) was deposited using Pulsed Laser Deposition (PLD) with a KrF (λ = 248 nm) excimer laser. Insulating 10 mm × 5 mm × 0.5 mm MgO (001) single crystal substrates (MTI Corporation, 1-side polished) were employed in this work to minimize substrate leakage current during the conductivity measurement. For film deposition, the backside substrate temperature was kept at 850 °C (which approximately

corresponds to 650 °C film temperature) in an oxygen pressure of 20 mTorr. By applying 30000 laser pulses (5 Hz, 1.5 mJ/cm^2) to the LSF target, a LSF thin film of ca. 110 nm thickness was grown on the substrate. After deposition, 5 nm Ti followed by 100 nm Pt were deposited as electrical contacts onto the film surface using magnetron sputtering.

Thin-film characterization: Atomic force microscopy (AFM) images were collected on a Cypher S AFM Microscope with tapping mode, using a Bruker TESP-V2 AFM probe. The AFM characterization was done on the center of the sample to avoid edge effects. X-ray diffraction (XRD) measurements were conducted with Rigaku SmartLab X-ray diffractometer using Cu *K*-alpha 1 radiation.

Near-Ambient Pressure XPS (NAP-XPS) measurement: The *in-situ* NAP-XPS measurements were carried out at the IOS (23-ID-2) beamline of the National Synchrotron Light Source II (NSLS-II) at Brookhaven National Lab. The sample was placed on a ceramic button heater, with a K-type thermocouples mounted directly onto the surface for temperature measurements. The LSF films were preconditioned at 400° C in 0.2 Torr O_2 at the beginning of each measurement to remove adventitious carbon. At each temperature, we waited for 15 minutes before the data collection. As the NAP-XPS measurements took about around 25 minutes, the time spent at each temperature is around 40 minutes. The electrical measurements were conducted with a Keithley 2461 Sourcemeter, available at the beamline. During the NAP-XPS measurement, the in-plane electrical measurements were carried out in a 2-probe geometry on the LSF film. Representative current-voltage characteristics of the LSF films are shown in Supplementary Note 7. All the NAP-XPS spectra were quantified with CasaXPS software. The XPS peaks were fitted with a 30% Lorentz/Gaussian line shape over a Shirley background.

X-Ray Absorption Spectroscopy (XAS): *Ex-situ* XAS were collected by partial fluorescence yield (PFY) modes at the IOS beamline of NSLS-II. PFY spectra were collected at room temperature in an ultrahigh-vacuum chamber (base pressure, ~10^{-9} torr), using a Vortex silicon drift detector. *In-situ* XAS were collected using the partial electron yield (PEY) method at Beamline 9.3.2 of the Advanced Light Source (ALS), Lawrence Berkeley National Laboratory.

Scanning Transmission Electron Microscopy (STEM) - Energy Dispersive X-ray Spectroscopy (EDX) Characterization: LSF films were characterized using a state-of-the-art aberration corrected JEOL Grand ARM300CF STEM operated at 300 keV. This instrument is equipped with dual silicon drift detectors for energy dispersive spectroscopy (EDX) with total detector area of 200 mm^2. Gatan Microscopy Suite (GMS version 3) software was used for STEM-EDS elemental mapping using these EDS peaks: O K_α (0.52 keV), Fe K_α and K_β (6.40 keV and 7.06 keV respectively), La L_α and L_β (4.65 keV and 5.04 keV respectively), and Sr K_α and K_β (14.16 keV and 15.84 keV respectively). FFT analysis on the STEM images, using the Gatan Microscopy Suite and ImageJ, was also performed to identify the phases in the LSF exsolved film.

Finite Element Analysis (FEA): The Poisson – Boltzmann equation was solved to obtain the nanocomposite electrical conductivity. The LSF matrix was modeled as a homogeneous 100 nm^3 cube, while the nanoparticles and the percolating channels were idealized as homogeneous spheres (5 nm in radius) and cylinders (radius 1 nm and height 100 nm), respectively. The geometry of these two objects were set based on their average dimensions, which is quantified by the cross-sectional STEM imaging. In this model, the nanoparticles and percolating channels were randomly generated in the matrix without intersection. All the materials properties in the FEA modeling were homogeneous and isotropic. The FEA analysis was coded in MATLAB.

Magnetic Properties Characterization: The magnetic hysteresis loops were measured using a Digital Measurement System 7035B vibrating sample magnetometer (VSM) at room temperature. During the VSM measurement, the magnetic field was applied parallel to the sample surface (i.e., in-plane direction). The data processing procedure is presented in Supplementary Note 11.

ACKNOWLEDGMENT

The authors would like to thank the Exelon Corporation and the MIT Energy Initiative Seed Fund Program for supporting the work presented in this paper. This research used the synchrotron radiation facilities at the National Synchrotron Light Source II (IOS/23-ID-2 beamline), a U.S. Department of Energy (DOE) Office of Science User Facility operated for the DOE Office of Science by Brookhaven National Laboratory under Contract No. DE-SC0012704; and the Advanced Light Source which is supported by the DOE Office of Basic Energy Sciences under Contract No. DE-AC02-05CH11231. The authors acknowledge the use of UC Irvine's Materials Research Institute (IMRI) for all the STEM-EDS characterization work. JW thanks Dimitrios Fraggedakis (MIT) for the helpful discussions on the Hashin-Shtrikman bounds. JW thanks Andreas Nenning (TU Wien) for the assistance on the Van der Pauw measurements. WJB acknowledges UCI new faculty start-up funding. KS acknowledges support from US Department of Education Graduate Assistance in Areas of National Need (GAANN) Fellowship. CR and SN acknowledge support from NSF DMR 1419807.

AUTHOR CONTRIBUTION

J.W. and B.Y. conceived the experiment design. J.W. prepared the samples and analyzed the data. J.W., I.W., A.H., and E.J.C. carried out the synchrotron experiments. K.S. and W.B. conducted the STEM imaging. S.N. conducted the VSM measurement. J.W. conducted the finite element analysis. J.W. wrote the manuscript and all authors contributed to its revision. B.Y. supervised the project.

REFERENCES

1 Acosta, M., Baiutti, F., Tarancón, A. & MacManus-Driscoll, J. L. Nanostructured Materials and Interfaces for Advanced Ionic Electronic Conducting Oxides. *Advanced Materials Interfaces* **6**, 1900462, doi:10.1002/admi.201900462 (2019).

2 Chen, A., Su, Q., Han, H., Enriquez, E. & Jia, Q. Metal Oxide Nanocomposites: A Perspective from Strain, Defect, and Interface. *Advanced Materials* **31**, 1803241, doi:10.1002/adma.201803241 (2019).

3 Benel, C., Reisinger, T., Kruk, R. & Hahn, H. Cluster-Assembled Nanocomposites: Functional Properties by Design. *Advanced Materials* **31**, 1806634, doi:10.1002/adma.201806634 (2019).

4 Baiutti, F. *et al*. A high-entropy manganite in an ordered nanocomposite for long-term application in solid oxide cells. *Nature Communications* **12**, 2660, doi:10.1038/s41467-021-22916-4 (2021).

5 Chen, Y. *et al*. Electronic Activation of Cathode Superlattices at Elevated Temperatures – Source of Markedly Accelerated Oxygen Reduction Kinetics. *Advanced Energy Materials* **3**, 1221-1229, doi:https://doi.org/10.1002/aenm.201300025 (2013).

6 Guo, X. & Maier, J. Ionically Conducting Two-Dimensional Heterostructures. *Advanced Materials* **21**, 2619-2631, doi:https://doi.org/10.1002/adma.200900412 (2009).

7 Yao, H., Hsieh, Y.-P., Kong, J. & Hofmann, M. Modelling electrical conduction in nanostructure assemblies through complex networks. *Nature Materials* **19**, 745-751, doi:10.1038/s41563-020-0664-1 (2020).

8 Ohtomo, A. & Hwang, H. Y. A high-mobility electron gas at the LaAlO3/SrTiO3 heterointerface. *Nature* **427**, 423-426, doi:10.1038/nature02308 (2004).

9 Sata, N., Eberman, K., Eberl, K. & Maier, J. Mesoscopic fast ion conduction in nanometre-scale planar heterostructures. *Nature* **408**, 946-949, doi:10.1038/35050047 (2000).

10 Ramesh, R. & Spaldin, N. A. Multiferroics: progress and prospects in thin films. *Nature Materials* **6**, 21-29, doi:10.1038/nmat1805 (2007).

11 Ma, W. *et al*. Vertically aligned nanocomposite La0.8Sr0.2CoO3/(La0.5Sr0.5)2CoO4 cathodes – electronic structure, surface chemistry and oxygen reduction kinetics. *Journal of Materials Chemistry A* **3**, 207-219, doi:10.1039/C4TA04993D (2015).

12 Su, C., Wang, W., Liu, M., Tadé, M. O. & Shao, Z. Progress and Prospects in Symmetrical Solid Oxide Fuel Cells with Two Identical Electrodes. *Advanced Energy Materials* **5**, 1500188, doi:10.1002/aenm.201500188 (2015).

13 Wang, J., Li, L., Huyan, H., Pan, X. & Nonnenmann, S. S. Highly Uniform Resistive Switching in HfO2 Films Embedded with Ordered Metal Nanoisland Arrays. *Advanced Functional Materials* **29**, 1808430, doi:10.1002/adfm.201808430 (2019).

14 Yoon, J. H. *et al*. Highly Improved Uniformity in the Resistive Switching Parameters of TiO2 Thin Films by Inserting Ru Nanodots. *Advanced Materials* **25**, 1987-1992, doi:10.1002/adma.201204572 (2013).

15 Spring, J. *et al*. Toward Controlling Filament Size and Location for Resistive Switches via Nanoparticle Exsolution at Oxide Interfaces. *Small* **n/a**, 2003224, doi:10.1002/smll.202003224 (2020).

16 Hendrikse, H. C. *et al*. Shape-Preserving Chemical Conversion of Architected Nanocomposites. *Advanced Materials* **32**, 2003999, doi:https://doi.org/10.1002/adma.202003999 (2020).

17 Tsekouras, G., Neagu, D. & Irvine, J. T. S. Step-change in high temperature steam electrolysis performance of perovskite oxide cathodes with exsolution of B-site dopants. *Energy & Environmental Science* **6**, 256-266, doi:10.1039/C2EE22547F (2013).
18 Neagu, D., Tsekouras, G., Miller, D. N., Ménard, H. & Irvine, J. T. S. In situ growth of nanoparticles through control of non-stoichiometry. *Nature Chemistry* **5**, 916-923, doi:10.1038/nchem.1773 (2013).
19 Nishihata, Y. *et al*. Self-regeneration of a Pd-perovskite catalyst for automotive emissions control. *Nature* **418**, 164-167, doi:10.1038/nature00893 (2002).
20 Kousi, K., Tang, C., Metcalfe, I. S. & Neagu, D. Emergence and Future of Exsolved Materials. *Small* **n/a**, 2006479, doi:https://doi.org/10.1002/smll.202006479 (2021).
21 Munnik, P., de Jongh, P. E. & de Jong, K. P. Recent Developments in the Synthesis of Supported Catalysts. *Chemical Reviews* **115**, 6687-6718, doi:10.1021/cr500486u (2015).
22 Han, H. *et al*. Lattice strain-enhanced exsolution of nanoparticles in thin films. *Nature Communications* **10**, 1471, doi:10.1038/s41467-019-09395-4 (2019).
23 Kousi, K. *et al*. Low temperature methane conversion with perovskite-supported exo/endo-particles. *Journal of Materials Chemistry A* **8**, 12406-12417, doi:10.1039/D0TA05122E (2020).
24 Kousi, K., Neagu, D., Bekris, L., Papaioannou, E. I. & Metcalfe, I. S. Endogenous Nanoparticles Strain Perovskite Host Lattice Providing Oxygen Capacity and Driving Oxygen Exchange and CH4 Conversion to Syngas. *Angewandte Chemie International Edition* **59**, 2510-2519, doi:10.1002/anie.201915140 (2020).
25 Weber, M. L. *et al*. Exsolution of Embedded Nanoparticles in Defect Engineered Perovskite Layers. *ACS Nano*, doi:10.1021/acsnano.0c08657 (2021).
26 Lai, K.-Y. & Manthiram, A. Evolution of Exsolved Nanoparticles on a Perovskite Oxide Surface during a Redox Process. *Chemistry of Materials* **30**, 2838-2847, doi:10.1021/acs.chemmater.8b01029 (2018).
27 Dai, S., Zhang, S., Katz, M. B., Graham, G. W. & Pan, X. In Situ Observation of Rh-CaTiO3 Catalysts during Reduction and Oxidation Treatments by Transmission Electron Microscopy. *ACS Catalysis* **7**, 1579-1582, doi:10.1021/acscatal.6b03604 (2017).
28 Katz, M. B. *et al*. Reversible precipitation/dissolution of precious-metal clusters in perovskite-based catalyst materials: Bulk versus surface re-dispersion. *Journal of Catalysis* **293**, 145-148, doi:https://doi.org/10.1016/j.jcat.2012.06.017 (2012).
29 Neagu, D. *et al*. Nano-socketed nickel particles with enhanced coking resistance grown in situ by redox exsolution. *Nature Communications* **6**, 8120, doi:10.1038/ncomms9120 (2015).
30 Opitz, A. K. *et al*. Understanding electrochemical switchability of perovskite-type exsolution catalysts. *Nature Communications* **11**, 4801, doi:10.1038/s41467-020-18563-w (2020).
31 Lv, H. *et al*. In Situ Investigation of Reversible Exsolution/Dissolution of CoFe Alloy Nanoparticles in a Co-Doped Sr2Fe1.5Mo0.5O6−δ Cathode for CO2 Electrolysis. *Advanced Materials* **32**, 1906193, doi:10.1002/adma.201906193 (2020).
32 Dimitrakopoulos, G., Ghoniem, A. F. & Yildiz, B. In situ catalyst exsolution on perovskite oxides for the production of CO and synthesis gas in ceramic membrane reactors. *Sustainable Energy & Fuels* **3**, 2347-2355, doi:10.1039/C9SE00249A (2019).
33 Irvine, J. T. S. *et al*. Evolution of the electrochemical interface in high-temperature fuel cells and electrolysers. *Nature Energy* **1**, 15014, doi:10.1038/nenergy.2015.14 (2016).

34 Li, J. *et al*. Topotactic phase transformations by concerted dual-ion migration of B-site cation and oxygen in multivalent cobaltite La–Sr–Co–Ox films. *Nano Energy*, 105215, doi:https://doi.org/10.1016/j.nanoen.2020.105215 (2020).

35 Kwon, O. *et al*. Exsolution trends and co-segregation aspects of self-grown catalyst nanoparticles in perovskites. *Nature Communications* **8**, 15967, doi:10.1038/ncomms15967 (2017).

36 Raman, A. S. & Vojvodic, A. Modeling Exsolution of Pt from ATiO3 Perovskites (A = Ca/Sr/Ba) Using First-Principles Methods. *Chemistry of Materials*, doi:10.1021/acs.chemmater.0c03260 (2020).

37 Wang, J. *et al*. Tuning Point Defects by Elastic Strain Modulates Nanoparticle Exsolution on Perovskite Oxides. *Chemistry of Materials* **33**, 5021-5034, doi:10.1021/acs.chemmater.1c00821 (2021).

38 Chen, D., Chen, C., Baiyee, Z. M., Shao, Z. & Ciucci, F. Nonstoichiometric Oxides as Low-Cost and Highly-Efficient Oxygen Reduction/Evolution Catalysts for Low-Temperature Electrochemical Devices. *Chemical Reviews* **115**, 9869-9921, doi:10.1021/acs.chemrev.5b00073 (2015).

39 Lupetin, P., Gregori, G. & Maier, J. Mesoscopic Charge Carriers Chemistry in Nanocrystalline SrTiO3. *Angewandte Chemie International Edition* **49**, 10123-10126, doi:https://doi.org/10.1002/anie.201003917 (2010).

40 Smith, C. R., Lang, A. C., Shutthanandan, V., Taheri, M. L. & May, S. J. Effects of cation stoichiometry on electronic and structural properties of LaNiO3. *Journal of Vacuum Science & Technology A* **33**, 041510, doi:10.1116/1.4922346 (2015).

41 Dieterich, W., Dürr, O., Pendzig, P., Bunde, A. & Nitzan, A. Percolation concepts in solid state ionics. *Physica A: Statistical Mechanics and its Applications* **266**, 229-237, doi:10.1016/s0378-4371(98)00597-4 (1999).

42 Lee, H. S., Findlay, S. D., Mizoguchi, T. & Ikuhara, Y. The effect of vacancies on the annular dark field image contrast of grain boundaries: A SrTiO3 case study. *Ultramicroscopy* **111**, 1531-1539, doi:https://doi.org/10.1016/j.ultramic.2011.08.013 (2011).

43 Twu, N. *et al*. Designing New Lithium-Excess Cathode Materials from Percolation Theory: Nanohighways in LixNi2–4x/3Sbx/3O2. *Nano Letters* **15**, 596-602, doi:10.1021/nl5040754 (2015).

44 Draber, F. M. *et al*. Nanoscale percolation in doped BaZrO3 for high proton mobility. *Nature Materials* **19**, 338-346, doi:10.1038/s41563-019-0561-7 (2020).

45 Kim, Y. *et al*. Stretchable nanoparticle conductors with self-organized conductive pathways. *Nature* **500**, 59-63, doi:10.1038/nature12401 (2013).

46 Swanson, H. E. *Standard X-ray diffraction powder patterns*. Vol. 1 (US Department of Commerce, National Bureau of Standards, 1953).

47 Finger, L. W., Hazen, R. M. & Hofmeister, A. M. High-pressure crystal chemistry of spinel (MgAl 2 O 4) and magnetite (Fe 3 O 4): comparisons with silicate spinels. *Physics and Chemistry of Minerals* **13**, 215-220 (1986).

48 Schulz, D. & McCarthy, G. ICDD Grant-in-Aid. *North Dakota State University, Fargo, ND, USA* (1987).

49 Li, G., Lan, J. & Li, G. Chrysanthemum-like 3D hierarchical magnetic γ-Fe2O3 and Fe3O4 superstructures: facile synthesis and application in adsorption of organic pollutants from water. *RSC Advances* **5**, 1705-1711, doi:10.1039/C4RA10094H (2015).

50 Jian, W., Jia, R., Wang, J., Zhang, H.-X. & Bai, F.-Q. Iron oxides with a reverse spinel structure: impact of active sites on molecule adsorption. *Inorganic Chemistry Frontiers* **6**, 2810-2816, doi:10.1039/C9QI00790C (2019).

51 Neagu, D. *et al*. Demonstration of chemistry at a point through restructuring and catalytic activation at anchored nanoparticles. *Nature Communications* **8**, 1855, doi:10.1038/s41467-017-01880-y (2017).

52 Dann, S. E., Currie, D. B., Weller, M. T., Thomas, M. F. & Al-Rawwas, A. D. The Effect of Oxygen Stoichiometry on Phase Relations and Structure in the System La1-xSrxFeO3-δ ($0 \leqslant x \leqslant 1$, $0 \leqslant \delta \leqslant 0.5$). *Journal of Solid State Chemistry* **109**, 134-144, doi:https://doi.org/10.1006/jssc.1994.1083 (1994).

53 Qureshi, N., Ulbrich, H., Sidis, Y., Cousson, A. & Braden, M. Magnetic structure and magnon dispersion in LaSrFeO${}_{4}$. *Physical Review B* **87**, 054433, doi:10.1103/PhysRevB.87.054433 (2013).

54 Mohaddes-Ardabili, L. *et al*. Self-assembled single-crystal ferromagnetic iron nanowires formed by decomposition. *Nature Materials* **3**, 533-538, doi:10.1038/nmat1162 (2004).

55 Li, J., Yu, Y., Yin, Y.-M., Zhou, N. & Ma, Z.-F. A novel high performance composite anode with in situ growth of Fe-Ni alloy nanoparticles for intermediate solid oxide fuel cells. *Electrochimica Acta* **235**, 317-322, doi:https://doi.org/10.1016/j.electacta.2017.03.103 (2017).

56 Götsch, T. *et al*. Treading in the Limited Stability Regime of Lanthanum Strontium Ferrite—Reduction, Phase Change and Exsolution. *ECS Transactions* **91**, 1771-1781 (2019).

57 Mueller, D. N., Machala, M. L., Bluhm, H. & Chueh, W. C. Redox activity of surface oxygen anions in oxygen-deficient perovskite oxides during electrochemical reactions. *Nature Communications* **6**, 6097, doi:10.1038/ncomms7097 (2015).

58 Abbate, M. *et al*. Controlled-valence properties of La1-xSrxFeO3 and La1-xSrxMnO3 studied by soft-x-ray absorption spectroscopy. *Physical Review B* **46**, 4511-4519, doi:10.1103/PhysRevB.46.4511 (1992).

59 Kuhn, M., Hashimoto, S., Sato, K., Yashiro, K. & Mizusaki, J. Oxygen nonstoichiometry, thermo-chemical stability and lattice expansion of La0.6Sr0.4FeO3−δ. *Solid State Ionics* **195**, 7-15, doi:https://doi.org/10.1016/j.ssi.2011.05.013 (2011).

60 Marrocchelli, D., Bishop, S. R., Tuller, H. L. & Yildiz, B. Understanding Chemical Expansion in Non-Stoichiometric Oxides: Ceria and Zirconia Case Studies. *Advanced Functional Materials* **22**, 1958-1965, doi:https://doi.org/10.1002/adfm.201102648 (2012).

61 Frati, F., Hunault, M. O. J. Y. & de Groot, F. M. F. Oxygen K-edge X-ray Absorption Spectra. *Chemical Reviews* **120**, 4056-4110, doi:10.1021/acs.chemrev.9b00439 (2020).

62 Nakamura, T., Oike, R., Ling, Y., Tamenori, Y. & Amezawa, K. The determining factor for interstitial oxygen formation in Ruddlesden–Popper type La2NiO4-based oxides. *Physical Chemistry Chemical Physics* **18**, 1564-1569, doi:10.1039/C5CP05993C (2016).

63 Chen, C. T. *et al*. Electronic states in La2-xSrxCuO4 probed by soft-x-ray absorption. *Physical Review Letters* **66**, 104-107, doi:10.1103/PhysRevLett.66.104 (1991).

64 Thalinger, R., Gocyla, M., Heggen, M., Klötzer, B. & Penner, S. Exsolution of Fe and SrO Nanorods and Nanoparticles from Lanthanum Strontium Ferrite La0.6Sr0.4FeO3−δ Materials by Hydrogen Reduction. *The Journal of Physical Chemistry C* **119**, 22050-22056, doi:10.1021/acs.jpcc.5b06014 (2015).

65 Jeong, J. S. *et al*. Decomposition of La2−xSrxCuO4 into several La2O3 phases at elevated temperatures in ultrahigh vacuum inside a transmission electron microscope. *Physical Review Materials* **2**, 054801, doi:10.1103/PhysRevMaterials.2.054801 (2018).
66 Udomsilp, D. *et al*. High-Performance Metal-Supported Solid Oxide Fuel Cells by Advanced Cathode Processing. *Journal of The Electrochemical Society* **164**, F1375-F1384, doi:10.1149/2.0571713jes (2017).
67 Chen, M., Hu, Y., Chen, D., Hu, H. & Xu, Q. A novel anode for solid oxide fuel cells prepared from phase conversion of La0.3Sr0.7Fe0.7Cr0.3O3-δ perovskite under humid hydrogen. *Electrochimica Acta* **284**, 303-313, doi:https://doi.org/10.1016/j.electacta.2018.07.132 (2018).
68 Opitz, A. K. *et al*. The Chemical Evolution of the La0.6Sr0.4CoO3−δ Surface Under SOFC Operating Conditions and Its Implications for Electrochemical Oxygen Exchange Activity. *Topics in Catalysis* **61**, 2129-2141, doi:10.1007/s11244-018-1068-1 (2018).
69 Nenning, A. *et al*. Ambient Pressure XPS Study of Mixed Conducting Perovskite-Type SOFC Cathode and Anode Materials under Well-Defined Electrochemical Polarization. *The Journal of Physical Chemistry C* **120**, 1461-1471, doi:10.1021/acs.jpcc.5b08596 (2016).
70 Crumlin, E. J. *et al*. In Situ Ambient Pressure X-ray Photoelectron Spectroscopy of Cobalt Perovskite Surfaces under Cathodic Polarization at High Temperatures. *The Journal of Physical Chemistry C* **117**, 16087-16094, doi:10.1021/jp4051963 (2013).
71 Tsvetkov, N., Chen, Y. & Yildiz, B. Reducibility of Co at the La0.8Sr0.2CoO3/(La0.5Sr0.5)2CoO4 hetero-interface at elevated temperatures. *Journal of Materials Chemistry A* **2**, 14690-14695, doi:10.1039/C4TA01889C (2014).
72 Zhu, Y. *et al*. Tuning proton-coupled electron transfer by crystal orientation for efficient water oxidization on double perovskite oxides. *Nature Communications* **11**, 4299, doi:10.1038/s41467-020-17657-9 (2020).
73 Nenning, A. & Fleig, J. Electrochemical XPS investigation of metal exsolution on SOFC electrodes: Controlling the electrode oxygen partial pressure in ultra-high-vacuum. *Surface Science* **680**, 43-51, doi:https://doi.org/10.1016/j.susc.2018.10.006 (2019).
74 Yu, S. *et al*. Metal Nanoparticle Exsolution on a Perovskite Stannate Support with High Electrical Conductivity. *Nano Letters* **20**, 3538-3544, doi:10.1021/acs.nanolett.0c00488 (2020).
75 Opitz, A. K. *et al*. Water Splitting on Model-Composite La0.6Sr0.4FeO3- (LSF) Electrodes in H2/H2O Atmosphere. *ECS Transactions* **68**, 3333-3343, doi:10.1149/06801.3333ecst (2015).
76 Opitz, A. K. *et al*. Enhancing Electrochemical Water-Splitting Kinetics by Polarization-Driven Formation of Near-Surface Iron(0): An In Situ XPS Study on Perovskite-Type Electrodes. *Angewandte Chemie International Edition* **54**, 2628-2632, doi:10.1002/anie.201409527 (2015).
77 Zhou, J., Chen, Y., Chen, G., Wu, K. & Cheng, Y. Evaluation of LaxSr2−xFeO4 layered perovskite as potential electrode materials for symmetrical solid oxide fuel cells. *Journal of Alloys and Compounds* **647**, 778-783, doi:https://doi.org/10.1016/j.jallcom.2015.05.261 (2015).
78 Patrakeev, M. V. *et al*. Electron/hole and ion transport in La1−xSrxFeO3−δ. *Journal of Solid State Chemistry* **172**, 219-231, doi:https://doi.org/10.1016/S0022-4596(03)00040-9 (2003).

79 Kogler, S., Nenning, A., Rupp, G. M., Opitz, A. K. & Fleig, J. Comparison of Electrochemical Properties of La0.6Sr0.4FeO3-δThin Film Electrodes: Oxidizing vs. Reducing Conditions. *Journal of The Electrochemical Society* **162**, F317-F326, doi:10.1149/2.0731503jes (2015).
80 Goodenough, J. B. Theory of the Role of Covalence in the Perovskite-Type Manganites [La,M(II)]MnO3. *Physical Review* **100**, 564-573, doi:10.1103/PhysRev.100.564 (1955).
81 Shin, Y. *et al*. Effect of oxygen vacancies on electrical conductivity of La0.5Sr0.5FeO3−δ from first-principles calculations. *Journal of Materials Chemistry A* **8**, 4784-4789, doi:10.1039/C9TA12734H (2020).
82 Chiabrera, F. *et al*. Unraveling bulk and grain boundary electrical properties in La0.8Sr0.2Mn1−yO3±δ thin films. *APL Materials* **7**, 013205, doi:10.1063/1.5054576 (2018).
83 Hashin, Z. & Shtrikman, S. A variational approach to the theory of the elastic behaviour of multiphase materials. *Journal of the Mechanics and Physics of Solids* **11**, 127-140, doi:https://doi.org/10.1016/0022-5096(63)90060-7 (1963).
84 Chang, S. H. *et al*. Confined polaronic transport in (LaFeO3)n/(SrFeO3)1 superlattices. *APL Materials* **7**, 071117, doi:10.1063/1.5110190 (2019).
85 Adepalli, K. K., Yang, J., Maier, J., Tuller, H. L. & Yildiz, B. Tunable Oxygen Diffusion and Electronic Conduction in SrTiO3 by Dislocation-Induced Space Charge Fields. *Advanced Functional Materials* **27**, 1700243, doi:10.1002/adfm.201700243 (2017).
86 Chiabrera, F. *et al*. Engineering Transport in Manganites by Tuning Local Nonstoichiometry in Grain Boundaries. *Advanced Materials* **31**, 1805360, doi:10.1002/adma.201805360 (2019).
87 Bauer, U. *et al*. Magneto-ionic control of interfacial magnetism. *Nature Materials* **14**, 174-181, doi:10.1038/nmat4134 (2015).
88 Tan, A. J. *et al*. Magneto-ionic control of magnetism using a solid-state proton pump. *Nature Materials* **18**, 35-41, doi:10.1038/s41563-018-0211-5 (2019).
89 Bi, C. *et al*. Reversible Control of Co Magnetism by Voltage-Induced Oxidation. *Physical Review Letters* **113**, 267202, doi:10.1103/PhysRevLett.113.267202 (2014).
90 Tinti, V. B. *et al*. Exsolution of Nickel Nanoparticles from Mixed-Valence Metal Oxides: A Quantitative Evaluation by Magnetic Measurements. *Particle & Particle Systems Characterization* **37**, 1900472, doi:10.1002/ppsc.201900472 (2020).
91 Pussacq, T. *et al*. Nanometric nickel exsolution in the hexagonal perovskite Ba8Ta6NiO24: Survey of the structural, magnetic and catalytic features. *Journal of Alloys and Compounds* **766**, 987-993, doi:https://doi.org/10.1016/j.jallcom.2018.07.016 (2018).
92 Matsuura, H. *et al*. Influence of Oxidation and Size of Iron Nanoparticles on the Saturation Magnetization. *IEEE Transactions on Magnetics* **44**, 2804-2807, doi:10.1109/TMAG.2008.2002006 (2008).
93 Yoon, T.-J., Shao, H., Weissleder, R. & Lee, H. Oxidation Kinetics and Magnetic Properties of Elemental Iron Nanoparticles. *Particle & Particle Systems Characterization* **30**, 667-671, doi:https://doi.org/10.1002/ppsc.201300013 (2013).
94 Fang, Y. *et al*. Microstructure and Magnetic Studies of La1-xSrxFeO3 Nano Particles Fabricated by the Citrate Sol-Gel Method. *Materials Science* **25**, 231-237 (2019).
95 Shi, J. *et al*. Magnetic and optical absorption properties of the Fe:LaSrFeO4 composite film prepared by pulsed laser decomposition. *Journal of Alloys and Compounds* **663**, 880-884, doi:https://doi.org/10.1016/j.jallcom.2015.12.151 (2016).

96 Li, Q. *et al*. Correlation between particle size/domain structure and magnetic properties of highly crystalline Fe3O4 nanoparticles. *Scientific Reports* **7**, 9894, doi:10.1038/s41598-017-09897-5 (2017).
97 Ning, S. *et al*. Voltage Control of Magnetism above Room Temperature in Epitaxial SrCo1–xFexO3–δ. *ACS Nano*, doi:10.1021/acsnano.0c03750 (2020).
98 Myung, J.-h., Neagu, D., Miller, D. N. & Irvine, J. T. S. Switching on electrocatalytic activity in solid oxide cells. *Nature* **537**, 528-531, doi:10.1038/nature19090 (2016).
99 Chen, Z. *et al*. Organic Photochemistry-Assisted Nanoparticle Segregation on Perovskites. *Cell Reports Physical Science*, 100243, doi:https://doi.org/10.1016/j.xcrp.2020.100243 (2020).